

Bilateral-Fuser: A Novel Multi-cue Fusion Architecture with Anatomical-aware Tokens for Fovea Localization

Sifan Song, Jinfeng Wang, Zilong Wang, Shaopeng Wang, Jionglong Su[†], Xiaowei Ding[†], Kang Dang[†]

Abstract—Accurate localization of the fovea is a crucial initial step in analyzing retinal diseases since it helps prevent irreversible vision loss. Although current deep learning-based methods achieve better performance than traditional methods, they still face challenges such as inadequate utilization of anatomical landmarks, sensitivity to diseased retinal images, and various image conditions. In this paper, we propose a novel transformer-based architecture (Bilateral-Fuser) for multi-cue fusion. The Bilateral-Fuser explicitly incorporates long-range connections and global features using retina and vessel distributions to achieve robust fovea localization. We introduce a spatial attention mechanism in the dual-stream encoder to extract and fuse self-learned anatomical information. This design focuses more on features distributed along blood vessels and significantly reduces computational costs by reducing token numbers. Our comprehensive experiments demonstrate that the proposed architecture achieves state-of-the-art performance on two public datasets and one large-scale private dataset. Moreover, we show that the Bilateral-Fuser is more robust on both normal and diseased retina images and has better generalization capacity in cross-dataset experiments.

Index Terms—Fovea Localization, Vision Transformer, Dual-Stream Architecture, Multi-Cue Fusion

I. INTRODUCTION

The fovea, an anatomical landmark of the retina, is responsible for sharp central vision at the center of the macula [1]. Accurate detection of the macula and fovea is a crucial prerequisite for the diagnosis of several retinal diseases, *e.g.*, diabetic maculopathy and age-related macular degeneration [2]–[4]. The severity of vision loss is often related to the distance between the fovea and associated abnormalities, such as hemorrhages and exudates [4].

[†] Corresponding Authors.

This work was supported by the Key Program Special Fund in XJTLU (KSF-A-22).

Sifan Song, Jinfeng Wang and Jionglong Su are with School of AI and Advanced Computing, XJTLU Entrepreneur College (Taicang), Xi'an Jiaotong-Liverpool University, Suzhou, 215123, China (e-mail: {Sifan.Song19, Jinfeng.Wang20}@student.xjtlu.edu.cn, Jionglong.Su@xjtlu.edu.cn)

Zilong Wang and Kang Dang are with VoxelCloud, Inc., Los Angeles, California, 90024, USA (e-mail: {zlwang, kdang}@voxelcloud.net.cn)

Shaopeng Wang is with Zibo Central Hospital, Zibo, 255000, China (e-mail: 904268100@qq.com)

Xiaowei Ding is with Shanghai Jiao Tong University, Shanghai, 200240, China (e-mail: dingxiaowei@sjtu.edu.cn)

Early detection of the fovea location is important to prevent the irreversible damage to vision [3], [5], [6]. A robust method of fovea localization is crucial for downstream tasks in automated fundus diagnosis. However, several challenges to fovea localization remain. First, the dark appearance of fovea is indistinguishable from the color intensity of the surrounding retinal tissue, and local anatomical landmarks (*e.g.*, blood vessels) are absent in the vicinity of the fovea [4], [7], [8]. Second, the accuracy of fovea localization may be affected by the occurrence of retinal diseases [9]–[12]. For example, dark pathology caused by hemorrhages and microaneurysms may obscure the distinction between the fovea and retinal background. Bright lesions, such as exudates, may change the lightness of the fovea to bright rather than dark, leading to erroneous localization results. Third, poor light conditions and non-standard fovea locations during photography increase the difficulty of robust fovea localization [13]–[15]. Specifically, blurred and poorly illuminated photographs present challenges in estimating macula. For images where the optic disc (OD), rather than the macula, is centrally located, symmetry may lead to predictions opposite to the ground-truth. Therefore, a robust fovea localization method is necessary to model features of the entire image at a global scale.

Fortunately, other anatomical structures outside the fovea, such as blood vessels, are useful for localization [2]–[4], [7]–[10], [12], [15]–[20]. Previous works have utilized morphological methods to model the anatomical relationships between the fovea and blood vessels [2]–[4], [9], [12]. However, these morphological methods may fail when the image has rare fovea position and color intensity, as described above. Fovea localization is an important upstream task in clinical diagnosis, helping to diagnose maculopathy and abnormalities [2], [3]. Although recent works have employed deep learning methods to improve performance, they typically only utilize fundus images as input [11], [13], [14], [21]–[25]. These works are also implemented on datasets containing few challenging images, resulting in three main pitfalls: 1) inadequate exploitation of the anatomical structure outside the macula as only fundus images are used as input; 2) typical convolution-based architectures lacking incorporation of global features; and 3) sensitivity to challenging cases, such as rare fovea positions and severe lesions.

To address these challenges, we propose a novel architecture,

Bilateral-Fuser, which is an updated version of our previous work [15] (achieving best-paper-award finalist in *ISBI2022*). Inspired by TransFuser [26], we design a dual-stream encoder to fuse multi-cue features and a decoder to generate result maps. To utilize the anatomical structure outside the macula, the encoder's inputs are images from two different cues (*i.e.*, fundus and vessel distribution). We fuse the multi-cue features of fundus and vessel in four transformer-based modules, named Bilateral Token Incorporation (BTI), in the encoder. This design allows the modeling of global features and long-range connections for fovea localization, ensuring robust performance even in challenging images. Unlike TransFuser, it directly reduces and recovers token numbers, applying average pooling and bilinear interpolation methods, respectively. Such operations may lead to information loss. Thus we avoid information loss by applying TokenLearner [27] in the BTI module. The attention mechanism of TokenLearner extracts self-learning spatial information from both cues. Our design effectively exploits structural features along the optic disk and vessel distribution, and the attention mechanism reduces the number of tokens in the BTI module, significantly reducing computational effort.

Our work makes the following key contributions:

- We propose a novel dual-stream architecture for multi-cue fusion. Compared to typical convolutional-based fusion, this transformer-based structure globally incorporates long-range connections from multiple cues.
- We introduce the BTI module with learnable tokens to improve the efficiency of transformer-based fusion. The adaptive learning of tokens significantly reduces the token number from 1024 to 64. The spatial attention mechanism of the learnable tokens focuses more on features along the vessel distribution, leading to robust fovea localization.
- The proposed Bilateral-Fuser achieves state-of-the-art performance on three datasets (Messidor, PALM and Tisu) at only 25% computational cost (62.11G FLOPs) compared to the best previous work [15] (249.89G FLOPs). It also offers better performance and generalization capability in challenging cases.

II. RELATED WORK

A. Anatomical Structure-based Methods

Previous studies have typically relied on traditional image processing techniques to estimate fovea regions, as the approximate location of the macula is anatomically correlated with the optic disc (OD) and blood vessels [2]–[4], [9], [10], [12], [28]. The fovea center is located approximately 2.5 OD diameters from the center of the OD and is on the symmetric line of the main vessel branches that pass through the OD. These two features have been widely used for fovea localization [2], [4], [9], [10], [12], [28].

Some studies detect the fovea region based on OD location only. Narasimha *et al.* [10] propose a two-step approach that incorporates the distance from the OD center and the image

intensity to update the region of interest (ROI), and then locates the fovea center. Sekhar *et al.* [7] use the spatial relationship to select a sector-shaped candidate ROI. The boundary of the sector is 30 degrees above and below the line through the center of the image and OD. They then use a threshold to filter the intensity to estimate the fovea region. Blood vessels in color fundus images are relatively darker structures compared with OD. Some works utilize only the extracted the skeleton image of vessels to estimate ROI containing the macula. Deka *et al.* [3] and Medhi *et al.* [4] divide the image into several horizontal strips and select the ROI with respect to the absence of blood vessels in the neighborhood of the macula. They then utilize thresholds to detect macula. Guo *et al.* [12] propose a morphological method to fit the segmented skeleton of major vessels using a parabola. The line of symmetry of the parabola is used to localize the fovea region.

The OD and vessels have been widely utilized in fovea localization due to their anatomical relationship. Asim *et al.* [8] estimate ROI based on the pre-detected OD location and minimum intensity values, and exclude the ROI near the vascular tree to improve the accuracy. Li *et al.* [9], Aquino *et al.* [2] and Fu *et al.* [28] also use a parabolic fit of major vessels to detect the orientation of the macula and use the anatomical relationship (*i.e.*, distance) between OD and fovea center to estimate the approximate location. The difference is that Fu *et al.* [28] use a deep learning method (U-Net [29]) rather than an image processing method to detect OD and vessels. However, these methods based on anatomical features may underperform when processing pathological images. Additionally, they generally perform less competitively than more recent deep learning-based approaches.

Some attempts have been made to localize the macula without relying on anatomical features. For example, GeethaRamani and Balasubramanian [11] propose an approach to segment the macula using an unsupervised clustering algorithm. Pachade *et al.* [13] directly select the square in the middle of the image as ROI and use a filter on intensity for fovea localization. However, as these methods do not consider anatomical features, they may fail when the illumination is different or the macula is not found in a standard location (*i.e.*, the center of the image).

B. Deep Neural Networks in Fovea Localization

Deep learning has demonstrated superiority over traditional image processing and morphological techniques in many fields of medical image analysis, such as classification, segmentation and object localization [30]–[33]. Regarding the task of fovea localization, existing studies can be broadly classified into two categories: regression and segmentation.

Many deep learning-based methods formulate fovea localization as a regression task. Al-Bander *et al.* [22] and Huang *et al.* [24] propose a two-step regression approach that first predicts ROI and subsequently feeds the ROI into neural networks to localize the fovea center. Meyer *et al.* [23] and Bhatkalkar *et al.* [25] adopt pixel-wise distance or heatmap regression approaches for joint OD and fovea localization.

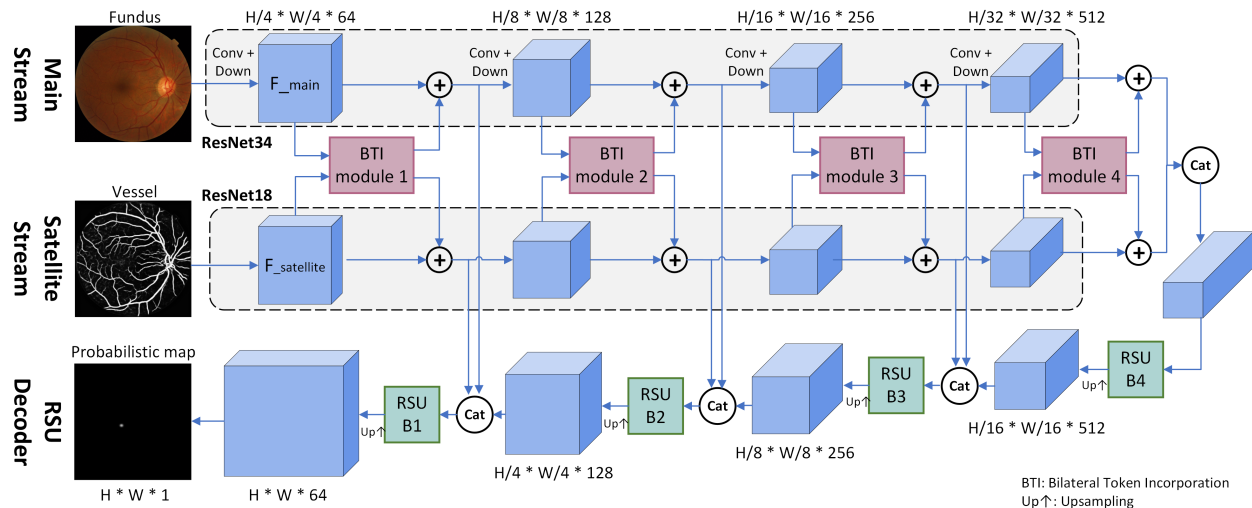


Fig. 1: The overall architecture of our proposed Bilateral-Fuser network.

Xie *et al.* [14] propose a hierarchical regression network that employs a self-attention mechanism in fovea localization [34], [35]. The network predicts the fovea center through a three-stage localization architecture that crops features from coarse to fine.

In addition to regression, deep learning-based methods also employ the image segmentation paradigm. Tan *et al.* [36] design a single 7-layer convolutional network to point-wise predict the fovea region from input image patches. Sedai *et al.* [21] propose a two-stage image segmentation framework for segmenting the fovea region from coarse to fine. However, standard CNN-based architectures are limited by their fixed-size convolutional kernels, resulting in a lack of incorporation of long-range features. Consequently, these CNN-based architectures may fail when light conditions and fovea positions are abnormal, or when information on the OD and vessels is lacking due to lesions.

To overcome the issue of limited receptive field, our previous work models long-range connections by proposing a two-branch segmentation architecture (Bilateral-ViT [15]), which utilizes a multi-head self-attention (MHSA) mechanism of transformer networks [37]–[39]. The main branch of Bilateral-ViT consists of 12 consecutive MHSA layers in the bottleneck, constituting the global features for the decoder. An additional vessel branch is designed to extract multi-scale spatial information from the vessel segmentation map as the second input. The decoder of Bilateral-ViT simultaneously fuses multi-cue features between the fundus and blood vessel distribution, achieving the best-reported results on two public datasets, Messidor [40] and PALM [41]. However, the multi-scale convolutional operation in the decoder has two main limitations, (1) non-global multi-cue feature fusion and (2) computationally expensive. To overcome these limitations, we propose a novel architecture, named Bilateral-Fuser, which includes an encoder for global-connected multi-cue fusion and introduce adaptively learnable tokens to reduce computational amount.

III. METHODOLOGY

In this study, we propose a novel multi-cue fusion architecture, Bilateral-Fuser (Fig. 1), for accurate and robust fovea localization. Bilateral-Fuser utilizes a U-shape architecture, where the encoder is a dual-stream structure comprising a main stream, a satellite stream, and four intermediate Bilateral Token Incorporation (BTI) modules for exploiting and fusing global features from different cues. For the decoder, we employ several ReSidual U-blocks (RSU) [31] to effectively incorporate features from both the main and satellite streams.

A. Overall Architecture

The overall architecture of Bilateral-Fuser is illustrated in Fig. 1. In the encoder, the backbones of the main and satellite streams are ResNet34 and ResNet18, respectively. The main stream extracts detailed features from fundus images, while the satellite stream extracts anatomical structure information from the distribution of blood vessels. Unlike the main stream, which takes fundus images as input, the satellite stream takes a vessel segmentation map generated by a pre-trained model as input. This pre-trained vessel segmentation model is built on the DRIVE dataset [42] using the TransUNet [39] architecture, which is identical to that used in [15].

The dual-stream encoder with four intermediate modules for multi-cue fusion is inspired by PVT [43] and TransFuser [26]. Each stream’s backbone is divided into four convolutional blocks, consisting of convolution and downsampling layers (Conv+Down). The resulting intermediate tensors (F_{main} and $F_{\text{satellite}}$) are then fed into the BTI module, which includes a TokenLearner, T consecutive Multi-Head Self-Attention (MHSA) layers, and a TokenFuser. The BTI module fuses multi-cue features and encodes long-range dependencies from both the fundus and vessel distribution. The output features are element-wise summed with skip-connected features and fed into the next convolution and downsampling layers. In addition,

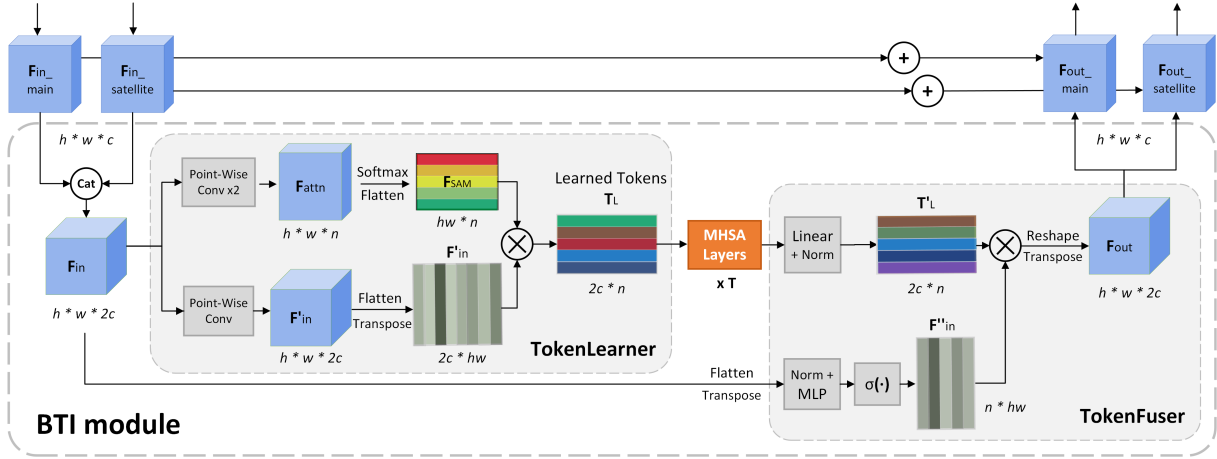


Fig. 2: The structure of BTI module used in our Bilateral-Fuser. It contains TokenLearner, $T \times$ MHSA layers and TokenFuser. The h , w and c are height, width, and channel of the corresponding input features. The n represents the number of learned tokens.

these output features from the BTI module are also forwarded to RSU blocks for subsequent decoding operations.

Unlike the commonly used plain convolutional blocks in the basic UNet decoder, four customized Residual U-blocks (RSU) [31] are utilized in the decoder of Bilateral-Fuser for effective multi-scale feature incorporation. The design of the RSU blocks is identical to that used in our previous work [15]. As shown in Fig. 1, RSU B4 is the bottleneck between the encoder and decoder. The input to the other three RSU blocks is a concatenation of three types of features: (i) multi-scale skip-connection features from the main stream, (ii) multi-scale skip-connection features from the satellite stream, (iii) the hidden feature decoded by the previous RSU block. Qin *et al.* [31] demonstrate that the RSU block is superior in performance to other embedded structures (*e.g.*, plain convolution, residual-like, inception-like, and dense-like blocks), due to the enlarged receptive fields of the embedded U-shape architecture. Moreover, the superiority of the RSU structure as the decoder for incorporating multiple features has also been assessed by [15].

B. Bilateral Token Incorporation (BTI) modules

Standard transformer/MHSA-based architectures, such as Vision Transformer (ViT) [38] and TransUNet [39], typically split the input image into 2D windows (*e.g.*, 16×16 grid) to generate tokens. The tokenization output is then fed into subsequent MHSA layers to model long-range feature connectivity. However, these tokens are extracted individually from a fixed-size grid. Recent architectures with multiple transformer stages [26], [43] have several times more MHSA layers than the standard ViT. The naive tokens extracted from the grids may contain uninformative or irrelevant features for visual understanding, which is computationally expensive.

To alleviate these pitfalls, the Bilateral Token Incorporation (BTI) module is introduced in the Bilateral-Fuser architecture (Fig. 2). The BTI module includes the TokenLearner [27],

which adaptively learns tokens using a spatial attention mechanism. After being processed by MHSA layers ($head = 8$ and $layer = 12$ for each BTI module), the tokens are remapped by TokenFuser [27] to the original input tensor dimensions (Fig. 2). Therefore, the BTI module has two main advantages: (1) generating adaptive and learnable tokens to reduce token numbers, and (2) merging and fusing features with long-range dependencies of both cues with high efficacy.

1) *TokenLearner*: Let $\mathbf{F}_{in_main} \in \mathbb{R}^{h \times w \times c}$ and $\mathbf{F}_{in_satellite} \in \mathbb{R}^{h \times w \times c}$ be the input tensors of the two streams, where h , w and c represent the height, width and channel of the corresponding BTI module. As shown in Fig. 2, the concatenated feature $\mathbf{F}_{in} \in \mathbb{R}^{h \times w \times 2c}$ is first fed into the TokenLearner. We customize the TokenLearner from [27] to generate $\mathbf{F}_{attn} \in \mathbb{R}^{h \times w \times n}$ using two consecutive point-wise convolutional layers to reduce the dimensionality, where n is the number of learned tokens. After applying the flatten and softmax functions, spatial attention maps with a dimension of $hw \times n$ are generated. Moreover, \mathbf{F}_{in} is processed by a point-wise convolutional layer, which is then flattened and transposed to become $\mathbf{F}'_{in} \in \mathbb{R}^{2c \times hw}$. To adaptively learn tokens using the spatial attention mechanism, the tokenization function is given by:

$$\mathbf{T}_L = \mathbf{F}'_{in} \mathbf{F}_{SAM} \quad (1)$$

$$\mathbf{F}_{SAM} = \text{softmax}(\text{flatten}(\mathbf{F}_{attn})) \quad (2)$$

where the learned tokens are denoted as $\mathbf{T}_L \in \mathbb{R}^{2c \times n}$. Because of the spatial attention mechanism, the learned tokens are modeled using an informative combination of corresponding spatial locations. In comparison to the 1024 tokens used in ViT and TransUNet [38], [39], we only retain 8×8 tokens for each BTI module (given an input size of 512×512). Since the computation of MHSA is quadratic to the number of tokens, the computational cost is significantly decreased. Therefore, TokenLearner enables us to not only significantly reduce the number of tokens but also extract features related to

the anatomical structure, *i.e.*, vessel distributions in this fovea localization task.

2) *TokenFuser*: As shown in Fig. 2, the resulting tokens from the the MHSA layers are recovered to their original tensor resolution ($h \times w \times 2c$) for further processing by Bilateral-Fuser. To fuse the information, we first utilize a fully-connected (linear) layer and output $\mathbf{F}'_{\text{L}} \in \mathbb{R}^{2c \times n}$. By processing \mathbf{F}_{in} simultaneously, the output tensor \mathbf{F}_{out} is given by:

$$\mathbf{F}_{\text{out}} = (\mathbf{T}'_{\text{L}} \mathbf{F}''_{\text{in}})^T \quad (3)$$

$$\mathbf{F}''_{\text{in}} = \sigma(\text{MLP}(\text{flatten}(\mathbf{F}_{\text{in}})^T)) \quad (4)$$

where tensors $\mathbf{F}_{\text{in}}, \mathbf{F}_{\text{out}} \in \mathbb{R}^{h \times w \times 2c}$ and $\mathbf{F}''_{\text{in}} \in \mathbb{R}^{n \times hw}$. $\sigma(\cdot)$ is a sigmoid function and MLP represents two dense layers with an intermediate GeLU activation function. In this case, the modeled tokens \mathbf{T}'_{L} are remapped to \mathbf{F}_{out} which has the same resolution as the initial \mathbf{F}_{in} . Following this, \mathbf{F}_{out} is equally split to $\mathbf{F}_{\text{out,main}}$ & $\mathbf{F}_{\text{out,satellite}}$ and added element-wise to the skip-connected features (*i.e.*, $\mathbf{F}_{\text{in,main}}$ & $\mathbf{F}_{\text{in,satellite}}$).

IV. EXPERIMENTS

A. Datasets and Network Configurations

We first conduct experiments using the *Messidor* [40] and *PALM* [41] datasets. The *Messidor* dataset was developed for analyzing diabetic retinopathy and comprises 540 normal and 660 diseased retinal images. For this dataset, we utilize 1136 images fovea locations provided by [16]. The *PALM* dataset was released for the Pathologic Myopia Challenge (PALM) 2019, which contains 400 images with fovea locations annotated. Of these, 213 images are pathologic myopia images, and the remaining 187 are normal retina images. For fairness of comparison, we follow the same data split as in the existing studies [14] and [15].

We also use a large-scale dataset (4103 images, named *Tisu*) which is collected from our cooperating hospital. All data have been desensitized with patients personal information removed. Compared to the *Messidor* and *PALM* datasets, *Tisu* is more challenging as it contains a larger number of fundus images with various abnormalities besides hemorrhages, microaneurysms, and exudates. The ground-truth fovea centers are determined by averaging the labels provided by three medical experts. The dataset is split into training and testing sets in a 4:1 ratio.

One of our main contributions is the considerable reduction in FLOPs and GPU usage of our proposed Bilateral-Fuser. Specifically, compared to the previous state-of-the-art Bilateral-ViT [15], our proposed Bilateral-Fuser consumes approximately 0.25 times FLOPs, 0.48 times GPU usage during training and 0.5 times GPU usage during inference. To evaluate whether the performance of Bilateral-ViT is caused by its large computational requirements, we have introduced a light version, Bilateral-ViT/Lit (*i.e.*, Bi-ViT/Lit in Table I). The basic architecture of Bilateral-ViT has been maintained, but we have reduced the number of middle channels in every convolutional block by half and decreased the number of tokens from 32×32

TABLE I: Configuration Comparison of Bilateral-ViT models and the proposed Bilateral-Fuser.

Methods	Tokens	Image Size	FLOPs	GPU/T ^a	GPU/T ^b
Bi-ViT [15]	32×32	512^2	249.89	16873	5459
Bi-ViT/Lit [15]	8×8	512^2	83.05	8653	3093
Bi-Fuser (Ours)	8×8	512^2	62.11	8083	2727

^a The GPU usage when training (MiB)

^b The GPU usage when inferencing (MiB)

to 8×8 . In this case, Bilateral-ViT/Lit has comparable FLOPs and GPU usage to our Bilateral-Fuser for a fair evaluation.

B. Implementation Details and Evaluation Metrics

To preprocess the fundus images, we first remove the uninformative black background, and then pad and resize the cropped image region to 512×512 . We simultaneously perform normalization and data augmentation on the input images of the main branch and the vessel branch. To train our Bilateral-ViT model, we generate circular fovea segmentation masks from the annotated fovea coordinates. During inference, we obtain a probabilistic map from the model's output by applying the sigmoid function. The final fovea location coordinates are obtained by calculating the median coordinates of all pixels in the map.

All experiments are implemented in PyTorch and conducted on one NVIDIA GeForce RTX TITAN GPU. We use the Adam optimizer [44] with a batch size of 2. The loss function is a combination of dice loss and binary cross-entropy. The experimental setup for the Bilateral-ViT architectures on *Messidor* and *PALM* datasets is the same as reported in [15]. For our proposed Bilateral-Fuser, we set the initial learning rate to $1e^{-3}$, which is gradually decayed to $1e^{-9}$ using the CosineAnnealingLR strategy over 300 epochs on *Messidor* and *PALM*. For the *Tisu* dataset, we set the initial learning rate to $6e^{-5}$ for all related experiments.

In accordance with the standard evaluation protocol, we adopt the following evaluation metrics to assess the performance of fovea localization [14]–[16], [23]: we consider the fovea localization to be successful if the Euclidean distance between the ground-truth and predicted fovea coordinates is no greater than a predefined threshold value, such as the radius of the optic disc R . To provide a comprehensive evaluation, we report the accuracy for different evaluation thresholds from $2R$ to $1/4R$ (*e.g.*, $2R$ indicating that the predefined threshold values are set to twice the radius of the optic disc R).

V. RESULTS

A. Comparison to State of the Art

In Table II, we compare the performance of Bilateral-Fuser with existing methods on the public dataset, *Messidor* and *PALM*. Methods are classified based on whether they use deep learning techniques and whether they incorporate multi-cue features. We observe that the traditional morphological methods [2], [16]–[20] rely on landmarks outside the macula, such as vessels or the optic disc. Bilateral-ViT [15] is the

TABLE II: Comparison with existing studies using the `Messidor` and `PALM` datasets based on the R rule. The best and second best results are highlighted in bold and italics respectively.

Messidor	DL ^a	MF ^b	1/4 R (%)	1/2 R (%)	1R (%)	2R (%)
Gegundez-Arias <i>et al.</i> (2013) [16]	✗	✓	76.32	93.84	98.24	99.30
Giachetti <i>et al.</i> (2013) [17]	✗	✓	-	-	99.10	-
Aquino (2014) [2]	✗	✓	83.01	91.28	98.24	99.56
Dashtbozorg <i>et al.</i> (2016) [18]	✗	✓	66.50	93.75	98.87	99.58
Girard <i>et al.</i> (2016) [19]	✗	✓	-	94.00	98.00	-
Molina-Casado <i>et al.</i> (2017) [20]	✗	✓	-	96.08	98.58	99.50
Al-Bander <i>et al.</i> (2018) [22]	✓	✗	66.80	91.40	96.60	99.50
Meyer <i>et al.</i> (2018) [23]	✓	✗	94.01	97.71	99.74	-
GeethaRamani <i>et al.</i> (2018) [11]	✓	✗	85.00	94.08	99.33	-
Pachade <i>et al.</i> (2019) [13]	✓	✗	-	-	98.66	-
Huang <i>et al.</i> (2020) [24]	✓	✗	70.10	89.20	99.25	-
Xie <i>et al.</i> (2020) [14]	✓	✗	98.15	99.74	99.82	100.00
Bhatkalkar <i>et al.</i> (2021) [25]	✓	✗	95.33	99.74	100.00	-
Bi-ViT (2022) [15]	✓	✓	98.59	100.00	100.00	100.00
Bi-ViT/Lit (2022) [15]	✓	✓	98.50	100.00	100.00	100.00
Bi-Fuser (Ours)	✓	✓	98.86	100.00	100.00	100.00
PALM	DL ^a	MF ^b	1/4 R (%)	1/2 R (%)	1R (%)	2R (%)
Xie <i>et al.</i> (2020) [14]	✓	✗	-	-	94	-
Bi-ViT (2022) [15]	✓	✓	65	83	96	98
Bi-ViT/Lit (2022) [15]	✓	✓	55	80	94	96
Bi-Fuser (Ours)	✓	✓	69	85	97	98

^a Whether the method is based on deep learning (DL).

^b Whether the method is based on multi-cue features (MF), e.g., fundus images, vessels or optical discs.

TABLE III: Comparison of performance on normal and diseased retinal images using the `Messidor` and `PALM` datasets. The best and second best results are highlighted in bold and italics respectively.

Messidor	MF ^a	FLOPs _↓	Err _↓	1/4 R(%)		1/2 R(%)		1R(%)		2R(%)	
				Normal	Diseased	Normal	Diseased	Normal	Diseased	Normal	Diseased
UNet (2015) [29]	✗	193.31	12.39	95.15	93.33	97.76	95.00	97.95	95.33	97.95	95.33
U2 Net (2020) [31]	✗	151.00	7.31	98.51	97.33	99.63	99.50	99.63	99.50	99.63	99.50
TransUNet (2021) [39]	✗	168.73	7.61	98.32	97.67	100.00	99.83	100.00	99.83	100.00	99.83
Bi-ViT (2022) [15]	✓	249.89	<i>6.81</i>	98.51	98.67	100.00	100.00	100.00	100.00	100.00	100.00
Bi-ViT/Lit (2022) [15]	✓	83.05	6.77	98.69	98.33	100.00	100.00	100.00	100.00	100.00	100.00
Bi-Fuser (Ours)	✓	62.11	6.77	99.07	98.67	100.00	100.00	100.00	100.00	100.00	100.00
PALM	MF ^a	FLOPs _↓	Err _↓	1/4 R(%)		1/2 R(%)		1R(%)		2R(%)	
				Normal	Diseased	Normal	Diseased	Normal	Diseased	Normal	Diseased
UNet (2015) [29]	✗	193.31	149.30	74.47	18.87	76.60	41.51	76.60	64.15	78.72	73.58
U2 Net (2020) [31]	✗	151.00	62.62	93.62	28.30	95.74	60.38	97.87	84.91	97.87	98.11
TransUNet (2021) [39]	✗	168.73	104.38	95.74	18.87	97.87	43.40	97.87	75.47	97.87	84.91
Bi-ViT (2022) [15]	✓	249.89	<i>53.70</i>	95.74	<i>37.74</i>	97.87	<i>69.81</i>	100.00	<i>92.45</i>	100.00	96.23
Bi-ViT/Lit (2022) [15]	✓	83.05	62.47	87.23	26.42	93.62	67.92	97.87	90.57	97.87	94.34
Bi-Fuser (Ours)	✓	62.11	48.72	95.74	45.28	97.87	73.58	100.00	94.34	100.00	96.23

^a Whether the method is based on multi-cue features (MF), e.g., fundus images, vessels or optical discs.

only previous deep learning-based method that incorporates fundus and vessel features. However, in most deep learning-based studies [11], [13], [14], [22]–[25], only fundus images are used, resulting in poor incorporation of anatomical relationships throughout the entire image, leading to failure in more challenging cases.

The proposed Bilateral-Fuser, which combines a transformer-based multi-cue fusion encoder and adaptive learning tokens, outperforms all previous studies in terms of fovea localization accuracy on the `Messidor` and `PALM` datasets. Specifically, in Table II, Bilateral-Fuser achieves the highest accuracy of 98.86% at $1/4R$, with gains of 0.71% and 3.53% compared to previous works [14] and [25], respectively. Our network also achieves better performance than Bilateral-ViT [15] and its light version. At evaluation thresholds of $1/2R$, $1R$, and

$2R$, Bilateral-Fuser achieves 100% accuracy, indicating a localization error of at most $1/2R$ (approximately 19 pixels for an input image size of 512×512).

The `PALM` dataset is more challenging, with a smaller number of images and complex diseased patterns. Our proposed Bilateral-Fuser demonstrates superiority over all other methods on this dataset in Table II, achieving accuracies of 69% and 85% at $1/4R$ and $1/2R$, respectively, which are 4% and 2% better than Bilateral-ViT. In addition, our method achieves a 14% improvement ($1/4R$) over Bilateral-ViT/Lit, and a 3% improvement ($1R$) over both Bilateral-ViT/Lit and [14]. Therefore, our Bilateral-Fuser achieves state-of-the-art performance on both `Messidor` and `PALM` datasets with high computational efficiency.

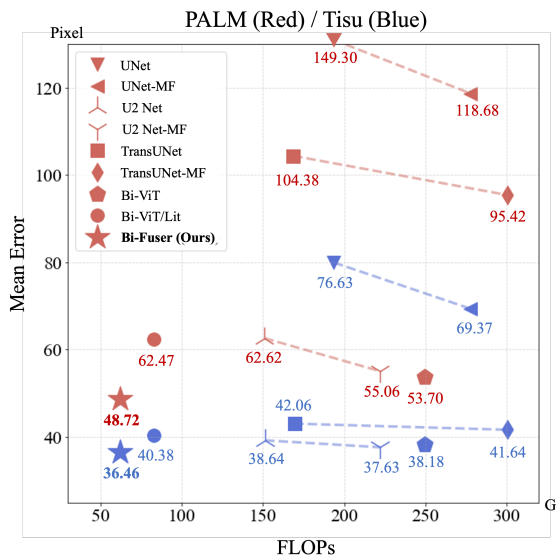


Fig. 3: Visualization of mean errors (Y-axis) of different multi-cue fusion models. X-axis is the computational cost (FLOPs). The red and blue markers are results on PALM and Tisu datasets, respectively. Numbers below the markers are corresponding mean errors.

B. Fovea Localization on Normal and Diseased Images

In Table III, we separately evaluate the performance of fovea localization for normal and diseased cases in Messidor and PALM datasets to assess the robustness of our method. We compare our proposed Bilateral-Fuser to several widely used segmentation networks, including UNet [29], U2 Net [31], and a hybrid version of TransUNet with ResNet50 for patch embedding [39]. The models of Bilateral-ViT, Bilateral-ViT/Lit and our Bilateral-Fuser are identical to those used in Table II.

In Table III, our proposed Bilateral-Fuser achieves the lowest error (Err) with the smallest computational cost (FLOPs) on both datasets. Bilateral-ViT [15] and our proposed Bilateral-Fuser both obtain 100% accuracy from 1/2R to 2R on all the Messidor images, and achieve 100% accuracy of 1R and 2R on normal PALM images. Compared to existing methods, Bilateral-Fuser demonstrates superior performance on almost all metrics on Messidor. Although Bilateral-Fuser has only 0.25 times FLOPs (62.11G) compared to Bilateral-ViT (249.89G), it achieves the best performance on diseased images of PALM from 1/4R to 2R, with up to 7.54% improvement compared to the other methods (1/4R, Diseased). Its improvement is significantly increased to 18.86% (1/4R, Diseased) compared to Bilateral-ViT/Lit (83.05G, *i.e.*, the network with the closest FLOPs to Bilateral-Fuser). Thus, our proposed Bilateral-Fuser is highly reliable in fovea localization on both normal and diseased fundus images with high efficacy.

C. Comparison of Multi-Cue Fusion Architectures

To comprehensively assess the performance of models with input features from multiple cues (fundus and vessel

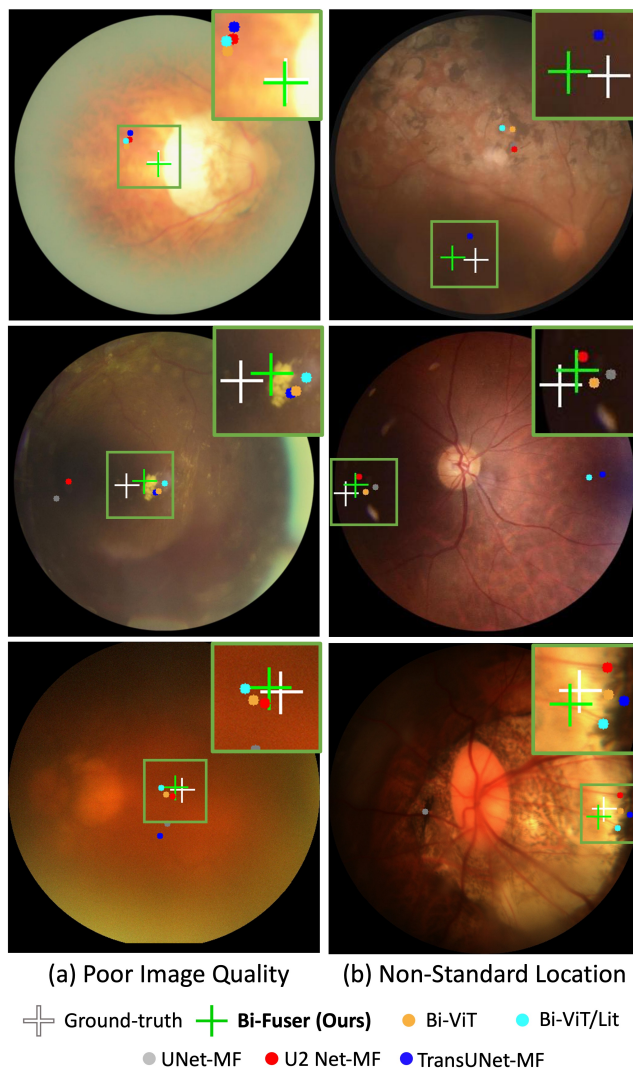


Fig. 4: Visual results of fovea localization predicted by different methods.

distributions), we implement a multi-cue fusion version for the baseline models, UNet, U2 Net and TransUNet. We utilize two identical encoders, each with an input of a fundus image and a vessel map. The features are extracted independently and concatenated at the bottleneck for decoding (similar to [26], [45]). These modified baseline models are referred to as UNet-MF, U2 Net-MF and TransUNet-MF. The results in Table III show that architectures using multi-cue features outperform typical networks with fundus-only input. This is particularly evident in the more challenging PALM dataset, where the improvement is more pronounced. Moreover, the Tisu dataset is more complex than PALM, with more images (4103 vs. 400) and a wider range of disease types and severity. Therefore, the results on PALM and Tisu demonstrate the potential of architectures that can effectively handle complex datasets.

Figure 3 shows a comparison of the described architectures (mean error against FLOPs) on PALM (red markers) and Tisu (blue markers). Below each marker, we provide the

TABLE IV: The performance of cross-dataset experiments. The models used here are exactly those selected in Fig. 3 (blue markers). **Top and Bottom:** The models trained on *Tisu* and tested on *PALM* and *Messidor*, respectively. The best and second best results are highlighted in bold and italics respectively.

<i>Tisu</i> → <i>Messidor</i>	Err _↓	1/4 R (%)	1/2 R (%)	1R (%)	2R (%)
UNet-MF (2015) [29]	8.89	97.45	99.38	99.65	99.65
U2 Net-MF (2020) [31]	8.48	97.10	99.91	100.00	100.00
TransUNet-MF (2021) [39]	8.25	97.45	99.82	100.00	100.00
Bi-ViT (2022) [15]	7.30	98.59	100.00	100.00	100.00
Bi-ViT/Lit (2022) [15]	7.37	98.06	99.91	100.00	100.00
Bi-Fuser (Ours)	7.62	98.59	99.91	100.00	100.00
<i>Tisu</i> → <i>PALM</i>	Err _↓	1/4 R (%)	1/2 R (%)	1R (%)	2R (%)
UNet-MF (2015)	137.14	52.25	64.25	77.25	85.50
U2 Net-MF (2020)	69.46	55.00	73.25	90.00	97.25
TransUNet-MF (2021)	78.98	53.50	71.75	87.50	95.75
Bi-ViT (2022) [15]	64.73	56.00	72.75	90.00	97.75
Bi-ViT/Lit (2022) [15]	71.14	55.50	73.25	90.75	97.00
Bi-Fuser (Ours)	59.21	55.25	73.25	93.50	98.50

corresponding mean error, and dashed lines connect each standard baseline model with its multi-cue fusion architecture (MF). The multi-cue fusion versions (UNet-MF, U2 Net-MF, and TransUNet-MF) outperform their standard versions at a considerably higher computational cost due to the additional encoder. In Fig. 3, we can see that the performance comparison (MF versions vs. baseline models) is more apparent on *PALM* since the dataset size of *PALM* is much smaller than *Tisu* (400 vs. 4103). For all multi-cue fusion architectures, our proposed Bilateral-Fuser achieves the best results with the smallest errors on both *PALM* (48.72 pixels) and *Tisu* (36.46 pixels). Moreover, it requires only 62.11G FLOPs, which is four times less than Bilateral-ViT (249.89G). Compared to the model with comparable FLOPs (Bilateral-ViT/Lit, 83.05G), Bilateral-Fuser shows significant advantages of 13.75 and 3.92 on *PALM* and *Tisu*, respectively.

Fig. 4 provides visual results of fovea localization on images with severe diseases from the *PALM* and *Tisu* datasets. These images in Fig. 4-a and Fig. 4-b suffer from poor image quality and non-standard fovea locations, respectively. Our Bilateral-Fuser generates the most accurate predictions for several challenging cases with poor lighting conditions and blurred appearance (Fig. 4-a). For another challenging types (Fig. 4-b), where the macula is close to the image boundary, the predictions of Bilateral-Fuser (green crosses) are closest to the ground-truth (white crosses). In contrast, fovea locations predicted by other architectures that cannot globally incorporate long-range multi-cue features may appear on the wrong side of the optic disc (Fig. 4-b). These results suggest that the Bilateral-Fuser architecture can adequately model fundus and vessel features of two streams, resulting in superior performance compared to other networks.

D. Performance of Cross-Dataset Experiments

We conduct cross-dataset experiments to assess the generalization capability of the proposed Bilateral-Fuser. In Table IV, models trained on *Tisu* (exactly the same ones in Fig. 3) are tested on *Messidor* and *PALM* datasets. In Table IV-**Top**, Bilateral-Fuser generally achieves similar accuracies as

TABLE V: Comparison of performance between different inputs for the main and satellite streams on *PALM* and *Tisu*. The best and second best results are highlighted in bold and italics.

<i>PALM</i>	Err _↓	1/4 R (%)	1/2 R (%)	1R (%)	2R (%)
Fundus+Vessel (Ours)	48.72	69	85	97	98
Fundus-only	54.46	64	85	95	98
Vessel-only	72.25	57	75	92	97
<i>Tisu</i>	Err _↓	1/4 R (%)	1/2 R (%)	1R (%)	2R (%)
Fundus+Vessel (Ours)	36.46	52.32	75.49	92.93	97.44
Fundus-only	37.48	52.32	73.78	91.10	96.95
Vessel-only	48.13	33.66	61.83	89.39	96.83

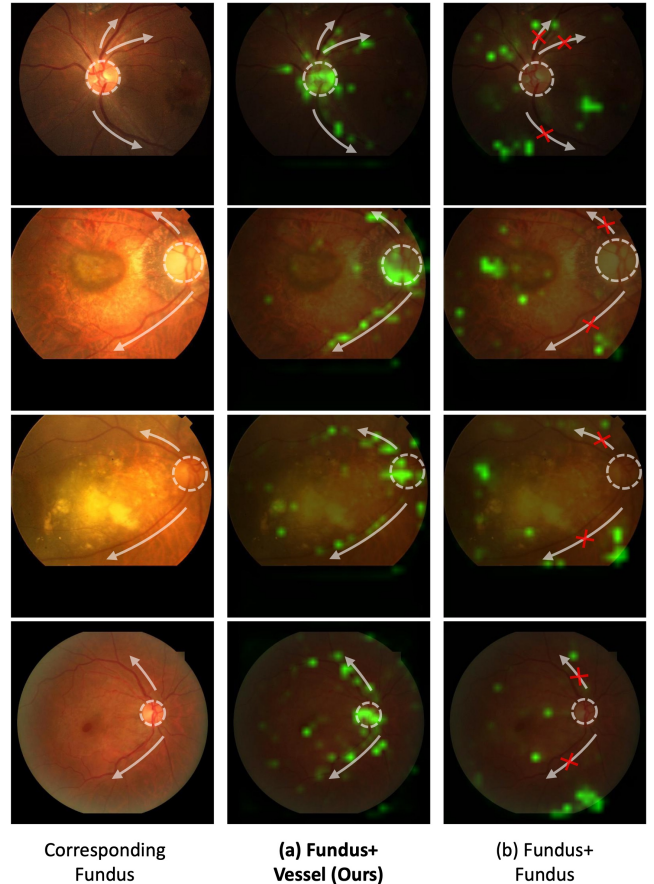


Fig. 5: Visualizations generated from spatial attention maps, indicating the focus of TokenLearner in BTI module. These visual results have been resized and superimposed onto the corresponding fundus.

the other results from 1/4R to 2R on *Messidor*. On the more challenging dataset, *PALM*, Bilateral-Fuser achieves an improvement of 5.52 and 11.93 pixels in average localization error at the original image resolution compared to Bilateral-ViT (64.73 pixels) and its lighter version (71.14 pixels), respectively (Table IV-**Bottom**). Furthermore, Bilateral-Fuser outperforms the baselines (multi-cue fusion version) by a significant margin (at least 10.25 pixels), demonstrating its excellent generalization capability and robustness.

E. Ablation Study

1) *Comparison of Inputs for Bilateral-Fuser:* Table V compares the performance of Bilateral-Fuser when using different

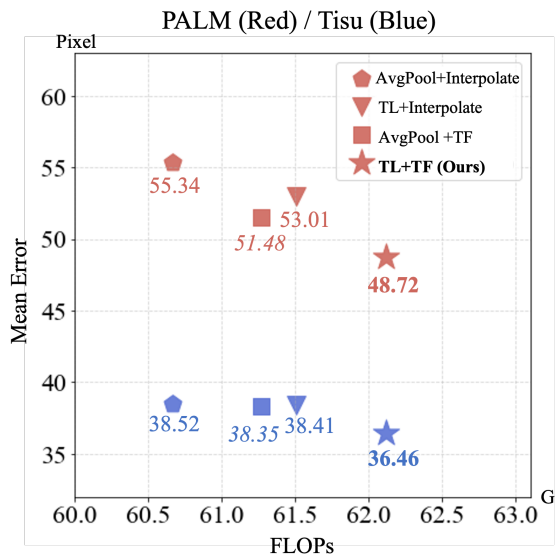


Fig. 6: Visualization of mean errors (Y -axis) of ablation studies for reducing and recovering tokens. X -axis is the computational cost (FLOPs). The red and blue markers are results on PALM and Tisu datasets, respectively. Numbers below the markers are corresponding mean errors.

inputs. The standard input configuration uses fundus images and vessel maps as inputs for the main and satellite streams, respectively (Fundus+Vessel). These experiments achieve the best accuracy on all metrics, with the smallest mean error on both PALM (48.72 pixels) and Tisu (36.46 pixels). When using fundus images as the second input (Fundus+Fundus), the model’s performance slightly degrades as feeding fundus images into the satellite stream does not provide the explicit anatomical structure for TokenLearner to learn where to focus its attention. Experiments using vessel maps as both inputs (Vessel+Vessel) lead to significant accuracy decreases on both PALM and Tisu by 23.53 and 11.67 pixels, respectively, indicating a severe loss of information.

As spatial attention maps reveal the self-learning features extracted by TokenLearners, we visually demonstrate these weight maps in Fig. 5. To visualize the attention of tokens in an element-wise manner, we maximize the probability values along the channels of spatial attention maps, and then normalize them. Finally, we superimpose these maps onto the corresponding fundus to compare their structural relationships.

Our experiments using Fundus+Vessel inputs show that the spatial attention maps focus on structural features along the optic disk and the direction of vessel branches (Fig. 5-a). This is feasible since these two structures have significant anatomical relationships with the fovea region [2], [7]–[10]. In contrast, although more detailed information is available to the Fundus+Fundus experiments, these TokenLearners, which are not guided by explicit anatomical structures, fail to learn features along the vessel distribution (Fig. 5-b). This leads to fewer tokens carrying useful features for fovea localization and may restrict the effectiveness of the intermediate BTI modules

in Bilateral-Fuser, resulting in slight underperformance on PALM and Tisu datasets (Table V). Therefore, the structural information provided by vessel maps as the second input is crucial for achieving accurate fovea localization.

2) *Comparison of Methods for Reducing and Recovering Tokens*: To evaluate the effectiveness of different components in reducing and recovering token numbers, we perform a comprehensive set of ablation experiments on the PALM and Tisu datasets. Instead of employing TokenLearner (TL) and TokenFuser (TF) with adaptively learnable parameters, we alternatively test more straightforward methods used in [26], average pooling (AvgPool) and bilinear interpolation (Interpolate), respectively.

In Fig. 6, we demonstrate a visualization of the mean error against the computational cost (FLOPs) on PALM (red) and Tisu (blue) datasets. Experiments using both TokenLearner and TokenFuser (TL+TF) achieve the best performance on PALM and Tisu with mean errors of 48.72 and 36.46 pixels, respectively. This is in contrast to using more straightforward methods such as average pooling (AvgPool) and bilinear interpolation (Interpolate), which may lead to a loss of information and reduced performance. In the proposed Bilateral-Fuser (TL+TF), total excess costs of FLOPs for the four BTI modules utilizing TokenLearner and TokenFuser are only **0.85G** and **0.61G**, respectively. This slight increase in computation leverages significant performance benefits, demonstrating the high efficacy of the adaptively learnable parameters of TokenLearner and TokenFuser in our architecture.

VI. CONCLUSIONS

Accurate detection of the macula and fovea is crucial for diagnosing retinal diseases. Although anatomical structures outside the fovea, such as the blood vessel distribution, are anatomically related to the fovea, relatively few recent deep learning approaches exploit them to improve the performance of fovea localization. In this paper, we propose a novel architecture, Bilateral-Fuser, which fuses features from the retina and corresponding vessel distribution with high efficacy for robust fovea localization. The Bilateral-Fuser contains a two-stream encoder for multi-cue fusion and a decoder for generating result maps. In addition, the Bilateral Token Incorporation (BTI) module in the encoder is designed to incorporate global anatomical features of inputs (both fundus and vessel images). Comprehensive experiments carried out demonstrate that the advantages of using Bilateral-Fuser with are more accurate localization results, insensitivity to diseased images, and low computational cost. Our proposed architecture achieves new state-of-the-art on two public datasets (Messidor and PALM) and one large-scale private dataset (Tisu) with metrics from $1/4 R$ to $2R$. It also outperforms other methods on cross-dataset experiments with better generalization capacity.

REFERENCES

- [1] J. Weiter, G. Wing, C. Trempe, and M. Mainster, “Visual acuity related to retinal distance from the fovea in macular disease.” *Annals of ophthalmology*, 1984.

- [2] A. Aquino, "Establishing the macular grading grid by means of fovea centre detection using anatomical-based and visual-based features," *Computers in biology and medicine*, 2014.
- [3] D. Deka, J. P. Medhi, and S. Nirmala, "Detection of macula and fovea for disease analysis in color fundus images," in *International Conference on Recent Trends in Information Systems (ReTIS)*, 2015.
- [4] J. P. Medhi and S. Dandapat, "An effective fovea detection and automatic assessment of diabetic maculopathy in color fundus images," *Computers in biology and medicine*, 2016.
- [5] K. S. Deepak and J. Sivaswamy, "Automatic assessment of macular edema from color retinal images," *IEEE Transactions on medical imaging*, vol. 31, no. 3, pp. 766–776, 2011.
- [6] L. Giancardo, F. Meriaudeau, T. P. Karnowski, Y. Li, S. Garg, K. W. Tobin Jr, and E. Chaum, "Exudate-based diabetic macular edema detection in fundus images using publicly available datasets," *Medical image analysis*, vol. 16, no. 1, pp. 216–226, 2012.
- [7] S. Sekhar, W. Al-Nuaimy, and A. K. Nandi, "Automated localisation of optic disk and fovea in retinal fundus images," in *2008 16th European Signal Processing Conference*, 2008.
- [8] K. M. Asim, A. Basit, and A. Jalil, "Detection and localization of fovea in human retinal fundus images," in *2012 International Conference on Emerging Technologies*, 2012.
- [9] H. Li and O. Chutatape, "Automated feature extraction in color retinal images by a model based approach," *IEEE Transactions on biomedical engineering*, 2004.
- [10] H. Narasimha-Iyer, A. Can, B. Roysam, V. Stewart, H. L. Tanenbaum, A. Majerovics, and H. Singh, "Robust detection and classification of longitudinal changes in color retinal fundus images for monitoring diabetic retinopathy," *IEEE transactions on biomedical engineering*, 2006.
- [11] R. GeethaRamani and L. Balasubramanian, "Macula segmentation and fovea localization employing image processing and heuristic based clustering for automated retinal screening," *Computer methods and programs in biomedicine*, 2018.
- [12] X. Guo, H. Wang, X. Lu, X. Hu, S. Che, and Y. Lu, "Robust fovea localization based on symmetry measure," *IEEE Journal of Biomedical and Health Informatics*, vol. 24, no. 8, pp. 2315–2326, 2020.
- [13] S. Pachade, P. Porwal, and M. Kokare, "A novel method to detect fovea from color fundus images," in *Computing, Communication and Signal Processing*. Springer, 2019.
- [14] R. Xie, J. Liu, R. Cao, C. S. Qiu, J. Duan, J. Garibaldi, and G. Qiu, "End-to-end fovea localisation in colour fundus images with a hierarchical deep regression network," *IEEE Transactions on Medical Imaging*, 2020.
- [15] S. Song, K. Dang, Q. Yu, Z. Wang, F. Coenen, J. Su, and X. Ding, "Bilateral-vit for robust fovea localization," in *2022 IEEE 19th International Symposium on Biomedical Imaging (ISBI)*. IEEE, 2022, pp. 1–5.
- [16] M. E. Gegundez-Arias, D. Marin, J. M. Bravo, and A. Suero, "Locating the fovea center position in digital fundus images using thresholding and feature extraction techniques," *Computerized Medical Imaging and Graphics*, 2013.
- [17] A. Giachetti, L. Ballerini, E. Trucco, and P. J. Wilson, "The use of radial symmetry to localize retinal landmarks," *Computerized Medical Imaging and Graphics*, 2013.
- [18] B. Dashtbozorg, J. Zhang, F. Huang, and B. M. ter Haar Romeny, "Automatic optic disc and fovea detection in retinal images using super-elliptical convergence index filters," in *International Conference on Image Analysis and Recognition*, 2016.
- [19] F. Girard, C. Kavalec, S. Grenier, H. B. Tahar, and F. Chérier, "Simultaneous macula detection and optic disc boundary segmentation in retinal fundus images," in *Medical Imaging 2016: Image Processing*, 2016.
- [20] J. M. Molina-Casado, E. J. Carmona, and J. García-Feijóo, "Fast detection of the main anatomical structures in digital retinal images based on intra-and inter-structure relational knowledge," *Computer methods and programs in biomedicine*, 2017.
- [21] S. Sedai, R. Tennakoon, P. Roy, K. Cao, and R. Garnavi, "Multi-stage segmentation of the fovea in retinal fundus images using fully convolutional neural networks," in *ISBI*, 2017.
- [22] B. Al-Bander, W. Al-Nuaimy, B. M. Williams, and Y. Zheng, "Multiscale sequential convolutional neural networks for simultaneous detection of fovea and optic disc," *Biomedical Signal Processing and Control*, 2018.
- [23] M. I. Meyer, A. Galdran, A. M. Mendonça, and A. Campilho, "A pixel-wise distance regression approach for joint retinal optical disc and fovea detection," in *MICCAI*, 2018.
- [24] Y. Huang, Z. Zhong, J. Yuan, and X. Tang, "Efficient and robust optic disc detection and fovea localization using region proposal network and cascaded network," *Biomedical Signal Processing and Control*, 2020.
- [25] B. J. Bhatkalkar, S. V. Nayak, S. V. Shenoy, and R. V. Arjunan, "Fundusposnet: A deep learning driven heatmap regression model for the joint localization of optic disc and fovea centers in color fundus images," *IEEE Access*, vol. 9, pp. 159 071–159 080, 2021.
- [26] A. Prakash, K. Chitta, and A. Geiger, "Multi-modal fusion transformer for end-to-end autonomous driving," in *Proceedings of the IEEE/CVF Conference on Computer Vision and Pattern Recognition*, 2021, pp. 7077–7087.
- [27] M. Ryoo, A. Piergiovanni, A. Arnab, M. Dehghani, and A. Angelova, "Tokenlearner: Adaptive space-time tokenization for videos," *Advances in Neural Information Processing Systems*, vol. 34, pp. 12 786–12 797, 2021.
- [28] Y. Fu, G. Zhang, J. Li, D. Pan, Y. Wang, and D. Zhang, "Fovea localization by blood vessel vector in abnormal fundus images," *Pattern Recognition*, vol. 129, p. 108711, 2022.
- [29] O. Ronneberger, P. Fischer, and T. Brox, "U-net: Convolutional networks for biomedical image segmentation," in *MICCAI*, 2015.
- [30] K. Suzuki, "Overview of deep learning in medical imaging," *Radiological physics and technology*, vol. 10, no. 3, pp. 257–273, 2017.
- [31] X. Qin, Z. Zhang, C. Huang, M. Dehghan, O. R. Zaiane, and M. Jagersand, "U2-net: Going deeper with nested u-structure for salient object detection," *Pattern Recognition*, vol. 106, 2020.
- [32] Q. Yu, K. Dang, N. Tajbakhsh, D. Terzopoulos, and X. Ding, "A location-sensitive local prototype network for few-shot medical image segmentation," in *ISBI*, 2021.
- [33] R. Yang and Y. Yu, "Artificial convolutional neural network in object detection and semantic segmentation for medical imaging analysis," *Frontiers in oncology*, vol. 11, p. 638182, 2021.
- [34] J. Cheng, L. Dong, and M. Lapata, "Long short-term memory-networks for machine reading," *arXiv preprint arXiv:1601.06733*, 2016.
- [35] H. Zhang, I. Goodfellow, D. Metaxas, and A. Odena, "Self-attention generative adversarial networks," in *International conference on machine learning*. PMLR, 2019, pp. 7354–7363.
- [36] J. H. Tan, U. R. Acharya, S. V. Bhandary, K. C. Chua, and S. Sivaprasad, "Segmentation of optic disc, fovea and retinal vasculature using a single convolutional neural network," *Journal of Computational Science*, vol. 20, pp. 70–79, 2017.
- [37] A. Vaswani, N. Shazeer, N. Parmar, J. Uszkoreit, L. Jones, A. N. Gomez, L. Kaiser, and I. Polosukhin, "Attention is all you need," *Advances in neural information processing systems*, vol. 30, 2017.
- [38] A. Dosovitskiy, L. Beyer, A. Kolesnikov, D. Weissenborn, X. Zhai, T. Unterthiner, M. Dehghani, M. Minderer, G. Heigold, S. Gelly *et al.*, "An image is worth 16x16 words: Transformers for image recognition at scale," *arXiv preprint arXiv:2010.11929*, 2020.
- [39] J. Chen, Y. Lu, Q. Yu, X. Luo, E. Adeli, Y. Wang, L. Lu, A. L. Yuille, and Y. Zhou, "Transunet: Transformers make strong encoders for medical image segmentation," *arXiv preprint arXiv:2102.04306*, 2021.
- [40] E. Decencière, X. Zhang, G. Cazuguel, B. Lay, B. Cochener, C. Trone, P. Gain, R. Ordonez, P. Massin, A. Erginay *et al.*, "Feedback on a publicly distributed image database: the messidor database," *Image Analysis & Stereology*, 2014.
- [41] H. Fu, F. Li, J. I. Orlando, H. Bogunovi, X. Sun, J. Liao, Y. Xu, S. Zhang, and X. Zhang, "Palm: Pathologic myopia challenge," 2019. [Online]. Available: <https://dx.doi.org/10.21227/55pk-8z03>
- [42] J. Staal, M. D. Abramoff, M. Niemeijer, M. A. Viergever, and B. Van Ginneken, "Ridge-based vessel segmentation in color images of the retina," *IEEE transactions on medical imaging*, 2004.
- [43] W. Wang, E. Xie, X. Li, D.-P. Fan, K. Song, D. Liang, T. Lu, P. Luo, and L. Shao, "Pyramid vision transformer: A versatile backbone for dense prediction without convolutions," in *Proceedings of the IEEE/CVF International Conference on Computer Vision*, 2021, pp. 568–578.
- [44] D. P. Kingma and J. Ba, "Adam: A method for stochastic optimization," *arXiv preprint arXiv:1412.6980*, 2014.
- [45] I. Sobh, L. Amin, S. Abdelkarim, K. Elmadawy, M. Saeed, O. Abdeltawab, M. Gamal, and A. El Sallab, "End-to-end multi-modal sensors fusion system for urban automated driving," 2018.